Neurosci. Bull. January, 2023, 39(1):57–68
https://doi.org/10.1007/s12264-022-00893-y

www.neurosci.cn
www.springer.com/12264

ORIGINAL ARTICLE

Mechanisms of PiT2-loop7 Missense Mutations Induced Pi Dyshomeostasis

Hao Sun[1] · Xuan Xu[2] · Junyu Luo[1] · Tingbin Ma[2] · Jiaming Cui[2] · Mugen Liu[1] · Bo Xiong[3] · Shujia Zhu[2] · Jing-Yu Liu[2]

Received: 12 February 2022 / Accepted: 14 April 2022 / Published online: 17 June 2022

Abstract PiT2 is an inorganic phosphate (Pi) transporter whose mutations are linked to primary familial brain calcification (PFBC). PiT2 mainly consists of two ProDom (PD) domains and a large intracellular loop region (loop7). The PD domains are crucial for the Pi transport, but the role of PiT2-loop7 remains unclear. In PFBC patients, mutations in PiT2-loop7 are mainly nonsense or frameshift mutations that probably cause PFBC due to C-PD1131 deletion. To date, six missense mutations have been identified in PiT2-loop7; however, the mechanisms by which these mutations cause PFBC are poorly understood. Here, we found that the p.T390A and p.S434W mutations in PiT2-loop7 decreased the Pi transport activity and cell surface levels of PiT2. Furthermore, we showed that these two mutations attenuated its membrane localization by affecting adenosine monophosphate-activated protein kinase (AMPK)- or protein kinase B (AKT)-mediated PiT2 phosphorylation. In contrast, the p.S121C and p.S601W mutations in the PD domains did not affect PiT2 phosphorylation but rather impaired its substrate-binding abilities. These results suggested that missense mutations in PiT2-loop7 can cause Pi dyshomeostasis by affecting the phosphorylation-regulated cell-surface localization of PiT2. This study helps understand the pathogenesis of PFBC caused by PiT2-loop7 missense mutations and indicates that increasing the phosphorylation levels of PiT2-loop7 could be a promising strategy for developing PFBC therapies.

Keywords PiT2-loop7 · Mutation · Primary familial brain calcification · Phosphorylation · Pi dyshomeostasis

Introduction

PiT2 is a member of the type III Na^+-dependent inorganic phosphate (Pi) transporter family [1, 2]. PiT2 was originally described as a retroviral receptor for the mouse leukemia virus (Ram-1) [3, 4] and was shown to be a Na^+-coupled Pi transporter [5, 6]. Loss-of-function mutations of solute carrier family 20 member 2 (*SLC20A2*) were linked to primary familial brain calcification (PFBC), and it was proposed that PFBC is caused by Pi dyshomeostasis [7].

PiT2 is composed of 652 amino acids [8]. There are two ProDom (PD) domains in PiT2: N-PD1131 (I_{11}–L_{161}) at the N-terminus and C-PD1131 (V_{492}–V_{640}) at the C-terminus [8, 9]. The extracellular loops in the PD domains, such as those formed by residues 67–91, 107–141, and 517–530, are required for retroviral receptor function [10, 11]. In addition, many amino-acid residues in the PD domains are crucial for the Pi transport function [9, 12]. Recently, a homologous protein structure of PiT2 from *Thermotoga maritima*

Hao Sun and Xuan Xu contributed equally to this work.

Supplementary Information The online version contains supplementary material available at https://doi.org/10.1007/s12264-022-00893-y.

✉ Shujia Zhu
shujiazhu@ion.ac.cn

✉ Jing-Yu Liu
liujy@ion.ac.cn

[1] College of Life Science and Technology, Huazhong University of Science and Technology (HUST), Wuhan 430074, China

[2] Institute of Neuroscience, State Key Laboratory of Neuroscience, Center for Excellence in Brain Science and Intelligence Technology, Chinese Academy of Sciences, Shanghai 200031, China

[3] Department of Forensic Medicine, Tongji Medical College, HUST, Wuhan 430030, China

(*Tm*PiT) was determined, providing new insights into the role of the PD domains in Pi transport [13]. During Pi transport, PiT2 shows an ordered binding sequence of Na^+:$H_2PO_4^-$:Na^+ [5, 14, 15]. The alternating-access transport mechanism is highly dependent on dynamic structural changes in the protein [16].

PiT2 also contains a large intracellular hydrophilic loop7 domain (PiT2-loop7) consisting of 246 amino acids (~ 38% of PiT2) between the two PD domains [8]. It has been suggested that the PiT2-loop7 domain might not participate in either retroviral recognition or Pi transport [9, 10]. In a previous study, we demonstrated that PiT2-loop7 participates in neuronal outgrowth by interacting with microtubule-associated protein 1B (MAP1B). Notably, PiT2-loop7 deletion results in the accumulation of PiT2 in the cytoplasm and a reduced level at the cell surface, indicating that PiT2-loop7 may be essential for the subcellular localization of PiT2 [17].

To date, ~ 145 mutations in *SLC20A2*, including 55 missense mutations, have been identified in PFBC patients [18–22]. Most of these mutations are located in the PD domains, reflecting their importance in Pi transport [21, 22]. Notably, six missense mutations (p.E267Q, p.S283R, p.R382Q, p.T390A, p.H399P, and p.S434W) have been identified in the loop7 region [18, 21, 23–25]. However, the detailed molecular mechanisms by which the missense mutations in PiT2 lead to PFBC remain unclear. In this study, we found that two missense mutations (p.T390A and p.S434W) in PiT2-loop7 caused a decrease in Pi transport *via* a mechanism involving phosphorylation-regulated cell-surface localization and two missense mutations (p.S121C and p.S601W) in the PD domains might lead to PiT2 dysfunction by altering its substrate-binding ability, possibly mediated by changes in protein structure.

Materials and Methods

Construction of Expression Plasmids

To construct mammalian and *Xenopus* expression plasmids, complementary DNA (cDNA) encoding human PiT2 (hPiT2) was cloned into the p3 × flag-CMV-7.1 and KSM vectors, respectively. After the wild-type (WT) vector was constructed, it was used as a template to generate the mutant constructs *via* site-directed mutagenesis. The authenticity of the plasmids was verified by Sanger sequencing. The primer information for site-directed mutagenesis is shown in Table S1.

Cell Culture and Transfection

Human embryonic kidney 293 (HEK293; ATCC, Manassas, USA) and COS7 (ATCC) cells were maintained in Dulbecco's modified Eagle's medium (DMEM; Gibco, New York, USA) supplemented with 10% fetal bovine serum (Gibco) at 37 °C under 5% CO_2. When cells were ~ 80% confluent, they were transfected with Hieff Trans™ liposomal transfection reagent (Yeasen, Shanghai, China) according to the manufacturer's protocol.

^{32}Pi Uptake Assay

HEK293 cells transfected with flag-tagged WT or mutant PiT2 were incubated at 37 °C for 24 h after transfection and were then cultured in phosphate-free DMEM (Gibco) for 12 h. Thereafter, the cells were incubated in phosphate-free DMEM containing 0.5 μCi/mL ^{32}Pi for 30 min, washed three times with ice-cold 0.9% NaCl, and lysed with 1% NP40. The lysates were then mixed with Ultima Gold (PerkinElmer, Waltham, USA), and the radioactivity was measured by scintillation counting. The cellular protein content was measured with a BCA Protein Assay Kit (Beyotime, Shanghai, China), and the cellular ^{32}Pi content was normalized to the cellular protein content. Pi influx was calculated as the ratio of cellular ^{32}Pi to the total amount of supplemented ^{32}Pi.

Homology Modeling

Predicted structural models of human PiT2 were generated *via* SWISS-MODEL [26] based on the structure of *Tm*PiT (PDB ID: 6L85) [13]. The structural changes were analyzed with PyMOL (The PyMOL Molecular Graphics System, Version 2.0, Schrödinger, LLC, New York, USA).

Complementary RNA (cRNA) Synthesis and Injection

KSM vectors were linearized by restriction digestion, purified by a standard method, and used as templates for capped cRNA synthesis using an mMESSAGE mMACHINE T3 kit (cat# AM1348, Ambion, Austin, USA). Stage V–VI oocytes were isolated, defolliculated, and injected with 50 nL (10 ng) of cRNA. The oocytes were incubated at 18°C in modified Barth's solution containing (in mmol/L) 88 NaCl, 1 KCl, 0.41 $CaCl_2$, 0.82 $MgSO_4$, 2.5 $NaHCO_3$, 2 $Ca(NO_3)_2$, and 7.5 HEPES-Tris (pH 7.4). Electrophysiological experiments were carried out 3–5 days after injection. Non-injected oocytes were used as negative controls.

Electrophysiology

Whole-cell currents were recorded using standard two-electrode voltage clamp equipment (Molecular Devices, Sunnyvale, USA), and data were acquired using pClamp 10.4 software (Molecular Devices). Microelectrodes were filled with 3 mol/L KCl, and the resistance varied from 0.5

to 3 MΩ. To determine the current–voltage (*I–V*) relationship, Pi-induced currents were measured from a holding potential of − 160 to + 60 mV in 20-mV increments. To examine Pi-induced currents, an oocyte was voltage-clamped at −60 mV and superfused with solution containing 100 mmol/L Na^+ (ND100 solution) at the beginning of each experiment. Then, the perfusate was switched to a perfusate containing 1 mmol/L Pi, and the change in the holding current was monitored. When the current reached a steady state, the perfusate was switched back, and Pi washout was monitored by recording the return of the holding current to baseline. The control superfusate was ND100 solution containing (in mmol/L): 100 NaCl, 2 KCl, 1.8 $CaCl_2$, 1 $MgCl_2$, and 10 HEPES (pH 7.4, adjusted with Tris). The test superfusate was ND100 solution containing 1 mmol/L Pi, which was added from 1 mol/L K_2HPO_4 and KH_2PO_4 stocks that were premixed to yield a pH of 7.4. To measure the affinities of WT and mutant PiT2 for Pi and Na^+, Pi-induced currents were measured under different conditions. To determine the affinity for Pi, the current induced by Pi at 0, 0.25, 0.50, 0.75, and 1.00 mmol/L was recorded at a constant concentration of Na^+ (100 mmol/L). To determine the affinity for Na^+, the current elicited by 1 mmol/L Pi with a variable concentration of Na^+ (0, 25, 50, 75, and 100 mmol/L) was recorded. The data obtained were normalized to the extrapolated maximum current elicited by 1 mmol/L Pi, and the half-maximal effective concentration (EC_{50}) values for Pi and Na^+ were calculated by fitting the normalized data to a modified Hill equation:

$$I = I_{\max}[S]^n/\{[S]^n+(EC_{50})^n\} \quad (1)$$

where I_{max} is the extrapolated maximum current, [*S*] is the concentration of Pi or Na^+, EC_{50} is the concentration of Pi or Na^+ that produces the half-maximal current, and *n* is the Hill coefficient.

Preparation of Total and Membrane Proteins

Total and membrane proteins were prepared as described previously [27, 28]. In brief, *Xenopus* oocytes (15 oocytes per group) were homogenized in 1 mL of protein isolation buffer containing (in mmol/L): 7.5 NaH_2PO_4, 250 sucrose, 5 EDTA, 5 EGTA (pH 7.0), and 1% protease inhibitor cocktail (cat# S8830, Sigma–Aldrich, St. Louis, USA). The homogenate was centrifuged at 3000× g for 10 min at 4 °C, after which the cell debris was removed; 100 μL of the supernatant was retained as total protein, and the remaining supernatant was ultracentrifuged at 100,000× g at 4 °C for 1 h. The pellet containing the membrane fraction was dissolved in 150 μL of protein resuspension buffer containing 20 mmol/L Tris-HCl, 5 mmol/L EDTA, and 5% sodium dodecyl sulfate (SDS) at pH 8.0. HEK293 cells transfected with WT or mutant PiT2 were transferred to phosphate-free DMEM after 24 h, cultured for another 12 h, and then incubated with 1 mmol/L Pi for 30 min. The cells were then harvested with ice-cold morpholinoethanesulphonic acid (MES) buffer containing 20 mmol/L MES, 200 mmol/L NaCl, 1 mmol/L phenylmethanesulfonyl fluoride (PMSF), and 1% protease inhibitor cocktail (cat# S8830, Sigma–Aldrich) at pH 6.0. Sonication was used to lyse the cells, and 100 μL of the lysate was retained as a total protein sample. The cell debris was removed from the remaining lysate *via* low-speed centrifugation at 3000× g for 10 min at 4 °C, and the supernatant was then ultracentrifuged at 100,000× g for 1 h at 4 °C. The membrane fragments were dissolved in 150 μL of MES buffer containing 1% N-dodecyl-β-D-maltoside (DDM). The total and membrane proteins were stored at − 80 °C until use.

Immunoprecipitation and Immunoblotting

Transfected HEK293 cells were harvested and lysed in 1 mL of MES buffer containing 1% DDM, and 100 μL of the lysate was retained as total protein. The remaining lysate was incubated with appropriate antibodies overnight at 4 °C. Then, protein A agarose beads (Merck Millipore, Darmstadt, Germany) were added, and the mixture was incubated for another 2 h. The beads were washed three times with MES buffer containing 0.02% DDM, and the immunoprecipitates were analyzed by immunoblotting. The protein samples were separated by 10% sodium dodecyl sulfate-polyacrylamide gel electrophoresis (SDS–PAGE) and transferred to nitrocellulose membranes. The membranes were incubated with 5% skim milk in TBST (150 mmol/L NaCl, 20 mmol/L Tris-HCl, 0.05% Tween 20; pH 7.4) for 2 h at room temperature and incubated with specific primary antibodies in 3% bovine serum albumin (BSA) at 4 °C overnight. The membranes were washed three times with TBST and then incubated with a horseradish peroxidase (HRP)-conjugated goat anti-mouse secondary antibody (1:10,000, Thermo Scientific, Waltham, USA) in 5% skim milk for 2 h at room temperature. After washing the membranes three times with TBST, the proteins were visualized using enhanced chemiluminescence reagents (ECL; Thermo Scientific). Protein expression was quantified with ImageJ (NIH, Bethesda, USA) software. The following primary antibodies were used: mouse anti-flag (MBL Life Science, Hokkaido, Japan; M185-3L), rabbit anti-flag (ABclonal, Wuhan, China; AE063), mouse anti-Na^+/K^+-ATPase (Santa Cruz Biotechnology, Santa Cruz, USA; sc-21712), mouse anti-β-actin (ABclonal, AC004), mouse anti-PiT2 (Santa Cruz Biotechnology, sc-101298), rabbit anti-PiT2 (ABclonal, A6739), rabbit anti-phospho (p)-AMPK substrate (CST, Boston, USA; 5759S), rabbit anti-p-AKT substrate (CST, 10001S), rabbit anti-p-AMPK (CST, 50081S), mouse anti-p-AKT

(Santa Cruz Biotechnology, sc-271966), rabbit anti-AMPK (CST, 2532S), rabbit anti-AKT (CST, 9272S), and mouse anti-phosphoserine (Santa Cruz Biotechnology, sc-81514).

Immunofluorescence Staining of Non-permeabilized Cells

HEK293 or COS7 cells transfected with WT or mutant PiT2 were transferred to phosphate-free DMEM after 24 h, cultured for another 12 h, and then incubated with 1 mmol/L Pi for 30 min. The cells were then fixed in 10% formaldehyde for 20 min and blocked with 5% BSA for 30 min at room temperature. Subsequently, the cells were incubated with flag antibody at 4 °C overnight. After washing three times with phosphate-buffered saline (PBS), the cells were incubated with Alexa Fluor 594-conjugated anti-mouse IgG (Life Technologies, Carlsbad, USA; A11020) as the secondary antibody at room temperature for 90 min. The nuclei were stained for 5 min with 4,6-diamidino-2-phenylindole (DAPI). Images were acquired using an Olympus FV1000 confocal microscope system (Olympus, Tokyo, Japan).

Statistical Analysis

Statistical analyses were performed by ordinary one-way analysis of variance (ANOVA) for comparisons among three or more groups. All data are presented as the mean ± SEM from at least three independent experiments, and differences were considered statistically significant at $P < 0.05$.

Results

Influences of Different Mutations on the Pi Transport Activity of PiT2

To explore the mechanisms by which different mutations in PiT2 cause PFBC, we selected p.T390A and p.S434W in the PiT2-loop7 and p.S121C and p.S601W in the PD domains as representative variants for investigation (Fig. 1A). We first applied Pi uptake assays to HEK293 cells expressing WT or mutant PiT2. All mutants showed markedly less Pi transport activity than WT PiT2. Notably, all mutants except p.S601W retained partial Pi transport activity (Fig. 1B). In addition, we carried out electrophysiological analyses of *Xenopus* oocytes expressing WT or mutant PiT2 (Fig. 1C–E). The slope conductance (G) provides an indicator of PiT2 activity. All mutants showed significantly reduced conductance compared with that of the WT (Fig. 1F). The reversal potential (E_{rev}) was shifted negatively in oocytes expressing the mutants (Fig. 1G). Moreover, the Pi-induced currents in oocytes expressing the mutants were lower than those in oocytes expressing the WT protein when the voltage was clamped to − 60 mV (Fig. 1H). These results suggested that these mutations in PiT2-loop7, similar to mutations in the PD domains, impair the Pi transport activity of PiT2.

Substrate-binding Properties of PiT2 Mutants

In previous studies, it has been proposed that disease-associated mutations might affect the substrate-binding ability of the transporters [13, 29, 30]. Therefore, we examined the affinities of WT and mutant PiT2 for Pi and Na^+. We obtained dose-response curves by recording Pi-induced currents in oocytes voltage-clamped at − 60 mV, and then normalized and plotted the current amplitude as a function of the Pi or Na^+ concentration (Fig. 2A, C). We then calculated the EC_{50} values of WT and mutant PiT2 for Pi and Na^+. The EC_{50} values of the p.T390A and p.S434W mutants for Pi and Na^+ were similar to the WT; in contrast, the EC_{50} values of the p.S121C and p.S601W mutants for Pi were increased and undetectable, respectively, while the EC_{50} values of these mutants for Na^+ were comparable to those of the WT (Fig. 2B, D). As the binding of substrates with transporters depends on crucial residues and particular conformations [30], we generated structural models of WT and mutant PiT2 using *Tm*PiT as a template. We found that residue 121 was near the possible transport channel and residue 601 was near the binding pocket of the substrates (Fig. 2E). In addition, the p.S121C mutation might abolish the hydrogen bond between residues 121 and 94 (Fig. 2F), and the p.S601W mutation might lead to a loss of the hydrogen bond between residues 601 and 574 (Fig. 2G). These results suggested that the p.S121C and p.S601W mutations might contribute to PiT2 dysfunction by affecting Pi-binding ability, possibly *via* effects on the structure of PiT2. However, these findings did not elucidate the mechanisms by which the p.T390A and p.S434W mutations lead to Pi dyshomeostasis.

Total and Cell Surface Expression Levels of the PiT2 Mutants

To determine how the two mutations in PiT2-loop7 disturb Pi homeostasis, we measured their total and cell-surface expression levels *in vitro*. HEK293 cells were transfected with plasmids expressing WT or mutant PiT2, and the total and membrane fractions were then prepared and analyzed by immunoblotting. The results revealed that the total expression levels of all the mutants were similar to that of WT PiT2, but the expression levels of the p.T390A and p.S434W mutants on the cell surface were significantly decreased (Fig. 3A, B). To further confirm that these two mutations affect the membrane localization of PiT2, we applied immunofluorescence staining to non-permeabilized

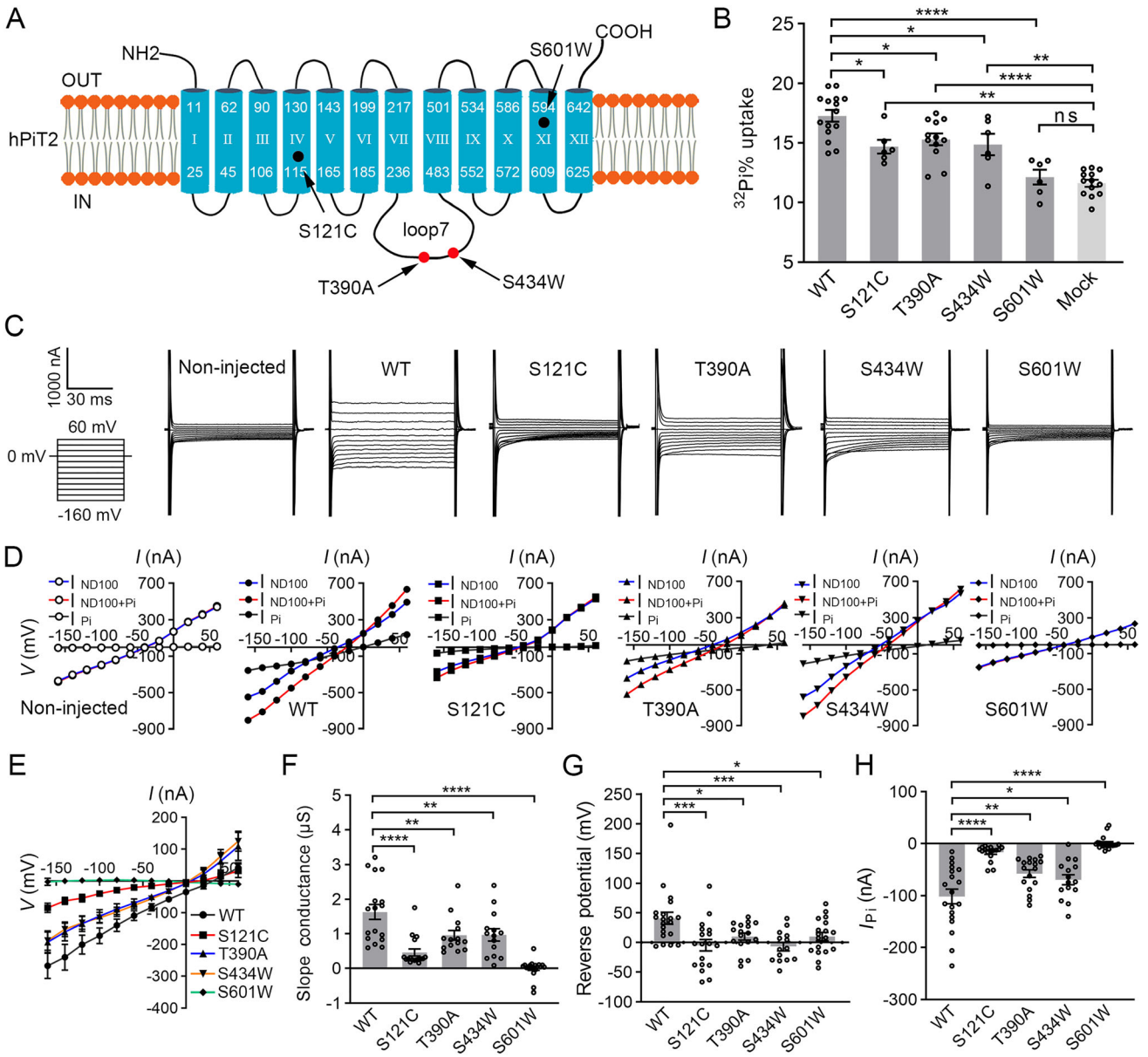

Fig. 1 Influences of different mutations on the Pi transport function of PiT2. **A** Schematic representation of the mutations of PiT2 characterized in this study. The mutated residues are indicated with black and red circles. **B** ^{32}Pi uptake assays of WT and mutant PiT2 in HEK293 cells (WT, $n = 15$; p.S121C, $n = 6$; p.T390A, $n = 12$; p.S434W, $n = 6$; p.S601W, $n = 6$; Mock, $n = 13$). All mutants show markedly less Pi transport activity than WT PiT2, but all mutants except p.S601W retain partial Pi transport activity. "Mock" indicates HEK293 cells transfected with empty vector as a negative control. **C** Representative current traces in oocytes expressing WT or mutant PiT2 upon application of 1 mmol/L Pi. **D** Representative *I–V* curves of oocytes expressing WT or mutant PiT2, first in ND100 solution (blue lines) and then in ND100 solution containing 1 mmol/L Pi (red lines). The Pi-dependent *I–V* curve (black lines) was generated by subtracting the current in ND100 from the current induced by Pi at the corresponding voltage (V_m). For the non-injected oocyte, the Pi-dependent *I-V* curve represents the background. **E** Dependence of the mean Pi-dependent current on V_m in oocytes expressing WT ($n = 20$), p.S121C ($n = 19$), p.T390A ($n = 18$), p.S434W ($n = 16$), or p.S601W ($n = 20$). **F** Conductance of *I–V* curves upon treatment with Pi for all groups in **E**. **G** Reversal potential in oocytes expressing WT or mutant PiT2 (WT, $n = 20$; p.S121C, $n = 19$; p.T390A, $n = 18$; p.S434W, $n = 16$; p.S601W, $n = 20$). **H** Pi-induced currents in oocytes expressing WT or mutant PiT2 when the voltage is clamped at − 60 mV (WT, $n = 19$; p.S121C, $n = 18$; p.T390A, $n = 17$; p.S434W, $n = 15$; p.S601W, $n = 19$). Data are presented as the mean ± SEM; $^*P < 0.05$, $^{**}P < 0.01$, $^{***}P < 0.001$, $^{****}P < 0.0001$, and "ns" indicates no significant difference, one-way ANOVA.

HEK293 or COS7 cells expressing WT or mutant PiT2. Compared with the WT, the p.T390A and p.S434W mutants showed clearly reduced membrane localization (Figs. 3C and S1). In addition, we applied similar tests to *Xenopus* oocytes. Consistently, all the mutants showed total expression levels similar to that of the WT, while the

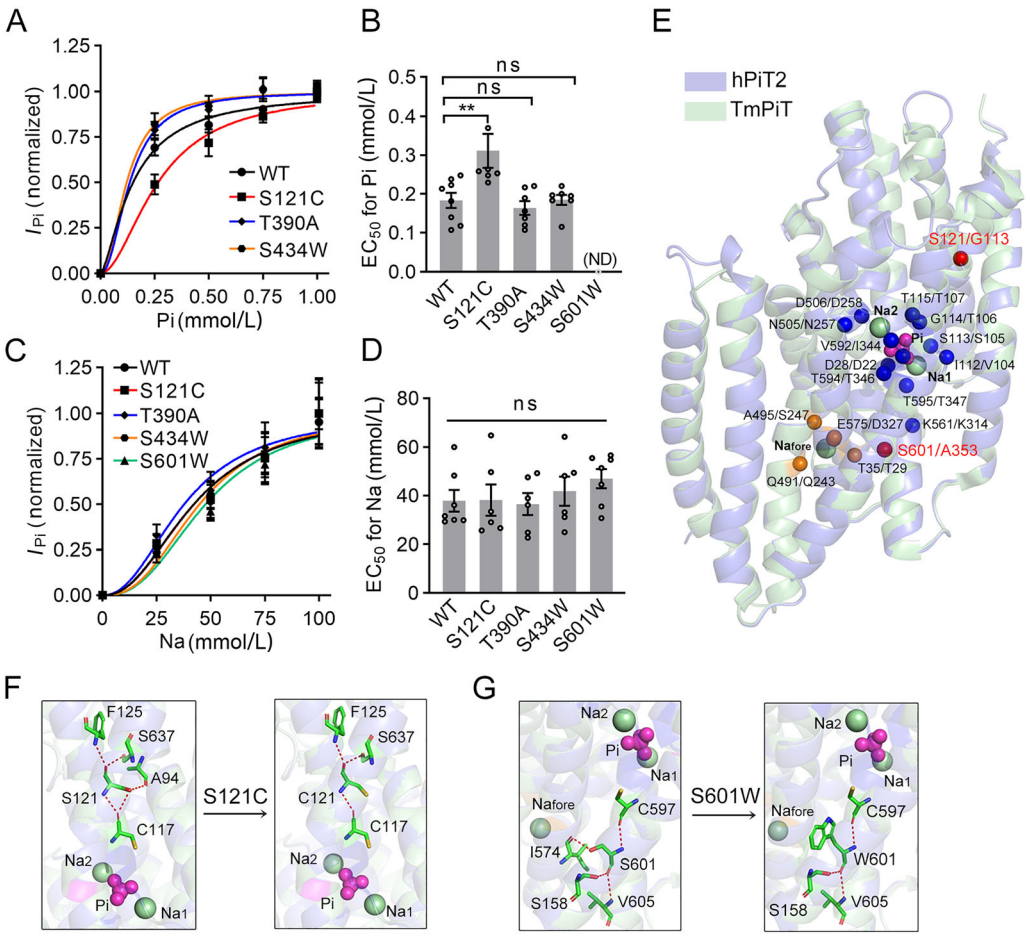

Fig. 2 Alterations in substrate-binding and structural models of PiT2 mutants. **A**, **C** Dose-response curves for Pi (WT, $n = 8$; p.S121C, $n = 7$; p.T390A, $n = 7$; p.S434W, $n = 7$) and Na^+ (WT, $n = 7$; p.S121C, $n = 6$; p.T390A, $n = 6$; p.S434W, $n = 6$; p.S601W, $n = 7$) in oocytes expressing WT or mutant PiT2. Data are normalized to the V_{max}, and the EC_{50} values were calculated by fitting the data to a modified Hill equation. **B**, **D** Quantitative analyses of the EC_{50} values of WT and mutant PiT2 for Pi (WT, $n = 8$; p.S121C, $n = 7$; p.T390A, $n = 7$; p.S434W, $n = 7$) and Na^+ (WT, $n = 7$; p.S121C, $n = 6$; p.T390A, $n = 6$; p.S434W, $n = 6$; p.S601W, $n = 7$). The EC_{50} values of the p.T390A and p.S434W mutants for Pi are similar to the WT, while those of the p.S121C and p.S601W mutants for Pi are increased or undetectable (ND), respectively (**B**). The EC_{50} values of these mutants for Na^+ are comparable to those of the WT (**D**). **E** Structural model of hPiT2 based on *Tm*PiT (green, Na^+; purple, Pi; blue, Pi- and Na^+-binding residues; orange, Na_{fore}-binding residues; red, mutation sites). Residue numbers are labeled as human/*Tm*. **F, G** Changes in the structural models of the p.S121C and p.S601W mutants. Data are presented as the mean ± SEM; $^{**}P < 0.01$ and "ns" indicates no significant difference, one-way ANOVA.

p.T390A and p.S434W mutants showed significantly decreased cell-surface expression (Fig. 3D, E). However, the p.S121C and p.S601W mutants showed total and cell-surface expression levels comparable to the WT (Figs. 3 and S1). These findings indicate that the p.T390A and p.S434W mutations interfere with Pi homeostasis by decreasing the cell-surface levels of PiT2.

The p.T390A and p.S434W Mutations Affect PiT2 Phosphorylation Associated with Membrane Localization

It has been reported that post-translational modifications (PTMs) participate in regulating the transport of membrane proteins to the cell surface [31, 32]. We hypothesized that the two mutation sites (T390 and S434) might be phosphorylation sites and PiT2 might undergo phosphorylation that is crucial for its membrane localization. To test this hypothesis, we first searched the potential protein kinases and found that the sequences in PiT2 surrounding T390 and S434 matched the sequences of the AMPK and AKT phosphorylation motifs [33–35], respectively, which are highly conserved among different species (Fig. 4A). To determine whether the two kinases are involved in PiT2 phosphorylation during Pi transport, we immunoprecipitated flag-PiT2-WT and analyzed its phosphorylation status with antibodies that recognize the phosphorylation motifs of AMPK (p-AMPK substrate antibody) or AKT (p-AKT substrate antibody). The immunoprecipitates preferentially reacted with the substrate antibodies of p-AMPK and

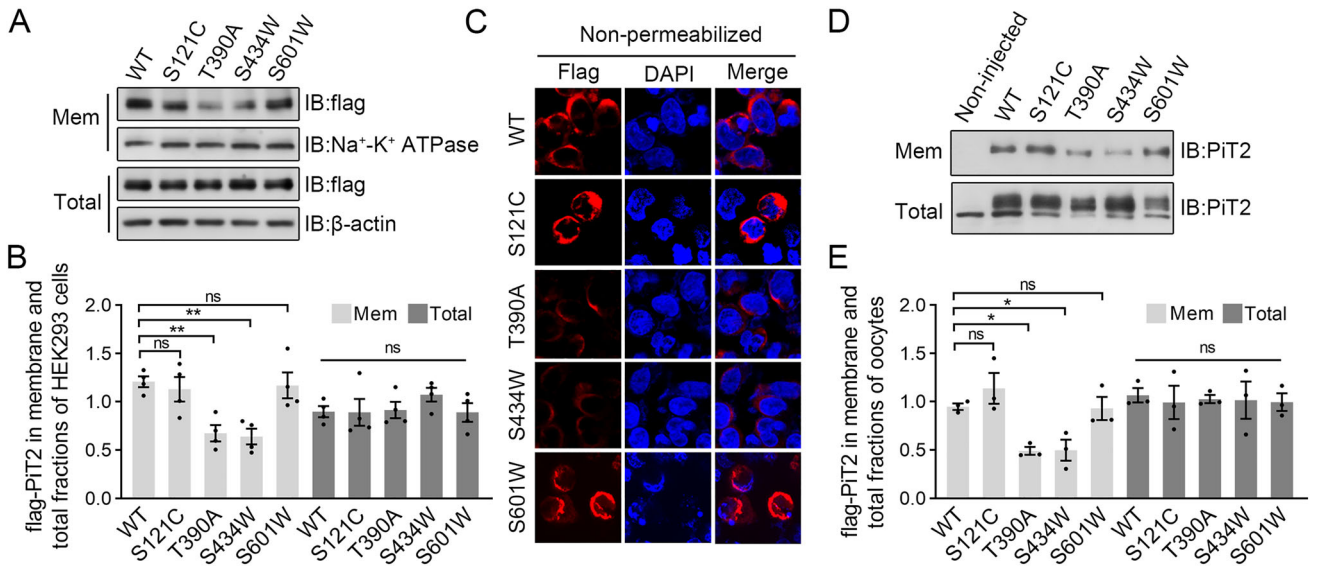

Fig. 3 Total and cell surface expression levels of WT and mutant PiT2. **A**, **D** Immunoblots of total and cell-surface expression levels of WT and mutant PiT2 using the indicated antibodies. The membrane (Mem) and total fractions were extracted from HEK293 cells or oocytes expressing WT and mutant PiT2. Na^+-K^+ ATPase and β-actin were used as cell surface and total protein controls in HEK293 cells, respectively. **B**, **E** Analysis of the immunoblotting data showing that the p.T390A and p.S434W mutations decrease the cell-surface expression level but do not affect the total expression level of PiT2, while the p.S121C and p.S601W mutations have no effect on the total and cell-surface expression levels of PiT2 (HEK293 cells, $n = 4$; oocytes, $n = 3$). **C** Non-permeabilized immunostaining of WT and mutant PiT2 in HEK293 cells. Data are presented as the mean ± SEM; $*P < 0.05$, $**P < 0.01$, one-way ANOVA.

p-AKT in Pi-treated cells, suggesting that AMPK and AKT mediate PiT2 phosphorylation during Pi transport (Fig. 4B, C, F, G). We also found that the interactions of activated AMPK and AKT with PiT2 were enhanced during Pi transport (Fig. 4B, D, F, H). Reciprocal co-immunoprecipitation assays further confirmed the interactions of PiT2 with AMPK and AKT (Fig. S2). To explore the association of PiT2 phosphorylation with its membrane localization, we purified the membrane fractions of HEK293 cells transfected with flag-PiT2-WT before and after Pi treatment and analyzed them by immunoblotting. The cell surface level of PiT2 was significantly increased after Pi treatment (Fig. 4B, E, F, I). Moreover, compound C and wortmannin, which are inhibitors of AMPK and AKT, respectively, inhibited all these changes (Fig. 4B–I). These results indicated that AMPK and AKT participate in PiT2 phosphorylation and promote its membrane localization.

To determine whether the p.T390A and p.S434W mutations are associated with the PiT2 phosphorylation status, we immunoprecipitated flag-tagged PiT2-WT, PiT2-T390A, and PiT2-S434W and analyzed the phosphorylation status using the substrate antibodies to p-AMPK (for T390A) and p-AKT (for S434W). Both the AMPK-mediated phosphorylation level of the p.T390A mutant (Fig. 4J, K) and the AKT-mediated phosphorylation level of the p.S434W mutant (Fig. 4L, M) were significantly lower than the phosphorylation level of the WT during Pi transport. In addition, we immunoprecipitated flag-tagged PiT2-WT, PiT2-S121C, and PiT2-S601W and assessed their phosphorylation status using an anti-phosphoserine antibody. The phosphorylation levels of the p.S121C and p.S601W mutants were comparable to those of the WT (Fig. S3). These results suggested that the p.T390A and p.S434W mutations affect PiT2 phosphorylation, thereby obstructing PiT2 transport to the cell surface.

Discussion

In this study, we found that PiT2-loop7 can be phosphorylated by AMPK and AKT and that its phosphorylation is positively associated with PiT2 membrane localization (Fig. 5A). The p.T390A and p.S434W mutations in PiT2-loop7 that cause PFBC could affect the phosphorylation of PiT2-loop7 and result in decreased cell surface expression of PiT2, eventually leading to a reduction in Pi transport (Fig. 5B). The p.S121C and p.S601W mutations in the PD domains could impair the Pi-binding ability of PiT2, thereby resulting in PiT2 dysfunction (Fig. 5C).

PTMs such as phosphorylation, methylation, glycosylation, and acetylation are critical for the structure, function, and kinetic properties of proteins [36–39]. For instance, protein kinase C (PKC)-mediated phosphorylation of glucose transporter 1 (GLUT1) on its cytoplasmic loop enhances GLUT1 cell-surface localization and facilitates GLUT1-mediated glucose uptake, and pathogenic

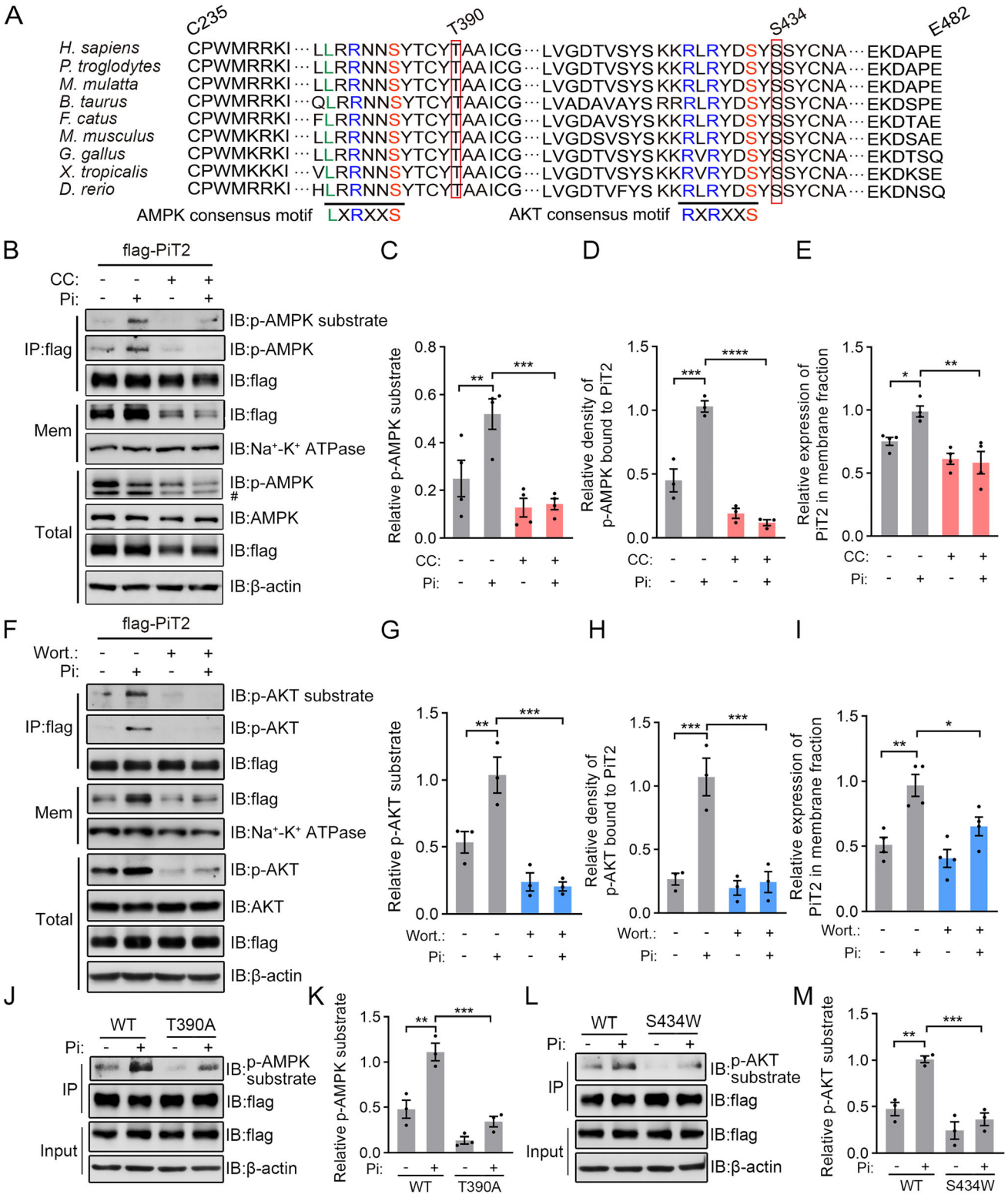
A
C235
T390
S434
E482
H. sapiens CPWMRRKI···LLRRNNSYTCYTAAICG···LVGDTVSYSKKRLRYDSYSSYCNA···EKDAPE
P. troglodytes CPWMRRKI···LLRRNNSYTCYTAAICG···LVGDTVSYSKKRLRYDSYSSYCNA···EKDAPE
M. mulatta CPWMRRKI···LLRRNNSYTCYTAAICG···LVGDTVSYSKKRLRYDSYSSYCNA···EKDAPE
B. taurus CPWMRRKI···QLRRNNSYTCYTAAICG···LVADAVAYSRRRLRYDSYSSYCNA···EKDSPE
F. catus CPWMRRKI···FLRRNNSYTCYTAAICG···LVGDAVSYSKKRLRYDSYSSYCNA···EKDTAE
M. musculus CPWMKRKI···LLRRNNSYTCYTAAICG···LVGDSVSYSKKRLRYDSYSSYCNA···EKDSAE
G. gallus CPWMKRKI···LLRRNNSYTCYTAAICG···LVGDTVSYSKKRVRYDSYSSYCNA···EKDTSQ
X. tropicalis CPWMKKKI···VLRRNNSYTCYTAAICG···LVGDTVSYSKKRVRYDSYSSYCNA···EKDKSE
D. rerio CPWMRRKI···HLRRNNSYTCYTAAICG···LVGDTVFYSKKRLRYDSYSSYCNA···EKDNSQ
AMPK consensus motif LXRXXS
AKT consensus motif RXRXXS
B
flag-PiT2
CC:
Pi:
IP:flag
Mem
Total
IB:p-AMPK substrate
IB:p-AMPK
IB:flag
IB:Na+-K+ ATPase
IB:p-AMPK #
IB:AMPK
IB:β-actin
C
Relative p-AMPK substrate
D
Relative density of p-AMPK bound to PiT2
E
Relative expression of PiT2 in membrane fraction
F
flag-PiT2
Wort.:
Pi:
IB:p-AKT substrate
IB:p-AKT
IB:AKT
G
Relative p-AKT substrate
H
Relative density of p-AKT bound to PiT2
I
Relative expression of PiT2 in membrane fraction
J
WT
T390A
IP
Input
IB:p-AMPK substrate
IB:flag
IB:β-actin
K
Relative p-AMPK substrate
L
WT
S434W
IB:p-AKT substrate
M
Relative p-AKT substrate

◀**Fig. 4** The p.T390A and p.S434W mutations affect AMPK- and AKT-mediated PiT2 phosphorylation associated with its membrane localization. **A** Sequence alignment of the phosphorylation motifs surrounding T390 and S434 in PiT2 orthologs of different species. **B** Immunoblots showing the correlation between AMPK and PiT2 phosphorylation and membrane localization in HEK293 cells expressing WT PiT2 using the indicated antibodies. # indicates a nonspecific band. **C–E** Quantitation of the immunoblotting data showing that the AMPK-mediated PiT2 phosphorylation (**C**, $n = 4$), the interaction of activated AMPK with PiT2 (**D**, $n = 3$), and the PiT2 membrane localization (**E**, $n = 4$) are significantly enhanced after treatment with Pi. The AMPK inhibitor, compound C (CC), inhibits all these changes. **F** Immunoblots showing the association of AKT with PiT2 phosphorylation and membrane localization using the indicated antibodies. **G–I** Quantitation showing that the AKT-mediated PiT2 phosphorylation (**G**, $n = 3$), the interaction of activated AKT with PiT2 (**H**, $n = 3$), and the PiT2 membrane localization (**I**, $n = 4$) increase following Pi treatment. The AKT inhibitor, wortmannin (wort.), counteracts these changes. **J**, **L** Immunoblots showing the influences of the p.T390A and p.S434W mutations on PiT2 phosphorylation with the indicated antibodies. **K**, **M** Quantitation of the phosphorylation levels of WT and mutant PiT2. The AMPK-mediated phosphorylation level of the p.T390A mutant (**K**, $n = 3$) and the AKT-mediated phosphorylation level of the p.S434W mutant (**M**, $n = 3$) are significantly lower than those of the WT. The data are presented as the mean ± SEM; $^{*}P < 0.05$, $^{**}P < 0.01$, $^{***}P < 0.001$, and $^{****}P < 0.0001$, one-way ANOVA.

mutations in the PKC motif that cause GLUT1 deficiency syndrome impair GLUT1 phosphorylation and ultimately block glucose uptake [31]. Methylation of Nav1.9 by protein arginine methyltransferase 7 (PRMT7) on the first intracellular loop increases the Nav1.9 current density by promoting its transport to the cell surface [32]. In this study, we found that PiT2-loop7 contains AMPK and AKT consensus motifs that may be accessible for phosphorylation, and we further confirmed that AMPK and AKT can mediate PiT2-loop7 phosphorylation. The results also demonstrated that the cell-surface expression of PiT2 was enhanced along with the phosphorylation of PiT2-loop7. Inhibition of AMPK or AKT resulted in decreased PiT2-loop7 phosphorylation accompanied by decreased PiT2 membrane localization. These results suggested that the phosphorylation of PiT2-loop7 mediated by AMPK and AKT is essential for PiT2 membrane localization (Fig. 4A–I). Among the PFBC-associated missense mutations in PiT2-loop7, the p.T390A and p.S434W mutations near the AMPK and AKT motifs, respectively, impaired PiT2-loop7 phosphorylation (Fig. 4A, J–M) and then obstructed PiT2 transport to the cell surface (Figs. 3 and S1). These findings indicate that the two mutations in PiT2-loop7 decrease Pi transport into cells by affecting the phosphorylation-regulated cell surface expression of PiT2. Four other missense mutations in PiT2-loop7 (p.E267Q, p.S283R, p.R382Q, and p.H399P) have been reported to cause PFBC [18, 21, 24]. The p.S283R, p.R382Q, and p.H399P mutations could impair the Pi transport activity of PiT2, whereas the p.E267Q variant could not (Fig. S4A). The p.R382Q mutation located in the AMPK motif might not only affect PiT2 expression but also obstruct its phosphorylation, resulting in decreased PiT2 membrane localization. The p.H399P mutation near the AMPK motif might only affect PiT2 phosphorylation, leading to a decrease in the cell-surface level of PiT2. Meanwhile, the p.E267Q and p.S283R mutations are far from the AMPK and AKT motifs and might not affect the PiT2 phosphorylation mediated by these two kinases; however, it is possible that the p.S283R mutation affects PiT2 phosphorylation mediated by other kinases, resulting in a reduction in PiT2 membrane localization (Fig. S4B–L). These results support the hypothesis that PiT2-loop7 missense mutations affect the phosphorylation-regulated membrane localization of PiT2, thereby leading to a decrease in Pi transport. Notably, the p.E267Q variant did not affect PiT2 expression, localization, or phosphorylation, which might explain why it did not affect Pi transport (Fig. S4). The p.E267Q variant was discovered in a PFBC family that also carried a deletion of exon 6 within *SLC20A2*; the real cause of PFBC in this family could be the deletion of exon 6 and not the p.E267Q variant [40].

Structural analyses of transporters can provide insights into their binding with substrates and their corresponding conformations and improve our understanding of the pathological mechanisms associated with disease-associated mutations [29, 41, 42]. Because the structure of human PiT2 remains unresolved, the specific effects of mutations are difficult to elucidate. Nevertheless, the recently-determined *Tm*PiT structure indicates that mutations in PiT2 might affect the binding of PiT2 with substrates and the corresponding conformation [13]. In this study, we found that the p.S121C and p.S601W mutations affected the Pi but not the Na^{+}-binding of PiT2 and might have varying effects on the structure of PiT2 (Fig. 2).

Many studies have revealed the importance of the PD domains in maintaining Pi transport [9, 12, 43, 44]. Most of the *SLC20A2* mutations are located in the PD domains [19], but it was unclear how these mutations affect Pi transport. In this study, we proposed that mutations in the PD domains might result in PiT2 dysfunction by affecting its substrate-binding ability and that different mutations could have diverse effects on PiT2 function, which might be associated with the different phenotypes in PFBC patients [23]. The clinical manifestations of PFBC patients with *SLC20A2* mutations, including those with PD domain mutations, mainly consist of movement disorders, cognitive decline, psychiatric symptoms, and headaches [22]. In this study, the p.S121C mutation resulted in partially reduced Pi transport activity of PiT2, while the p.S601W mutation resulted in a complete loss of its activity (Fig. 1).

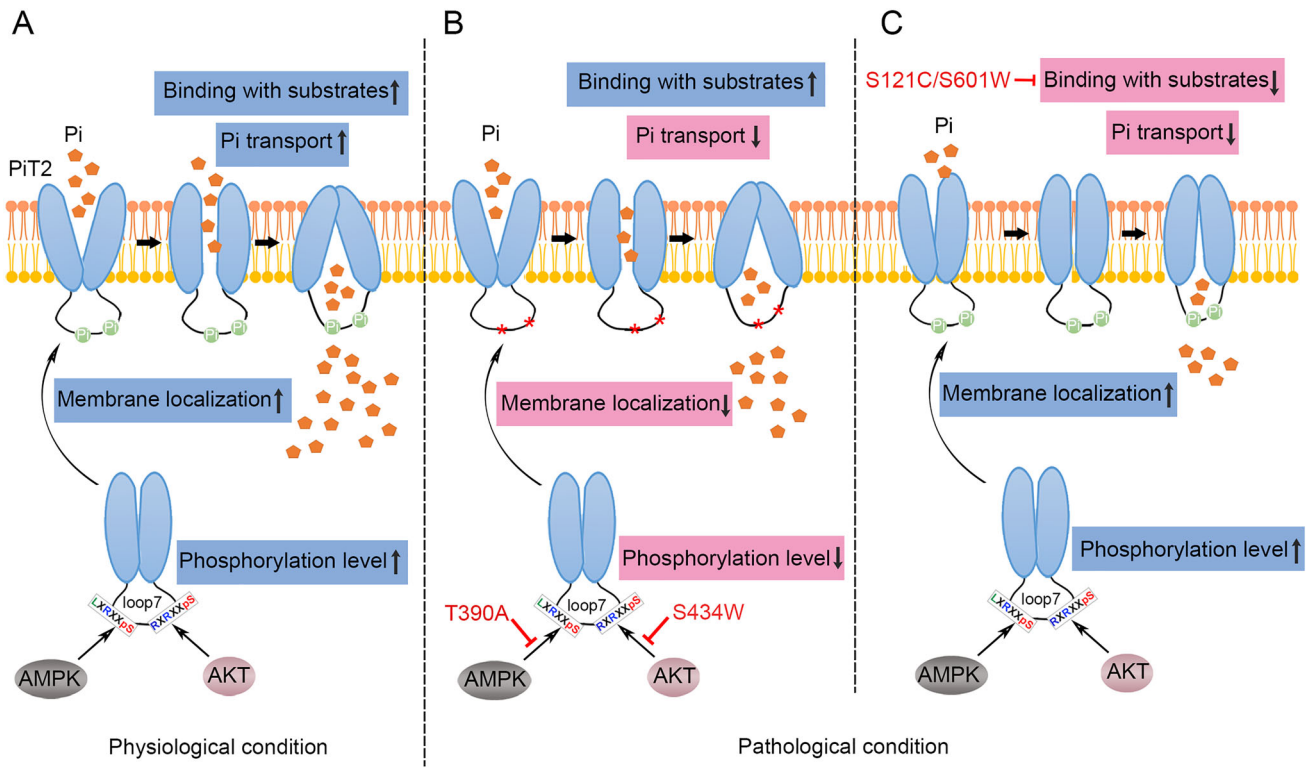

Fig. 5 Proposed model of how different mutations in PiT2 cause Pi dyshomeostasis. **A** Under physiological conditions, during Pi transport, activated AMPK or AKT binds to PiT2 and mediates its phosphorylation, eventually promoting PiT2 transport to the cell surface and PiT2 function. **B**, **C** Under pathological conditions, the p.T390A and p.S434W mutations in PiT2-loop7 affect the phosphorylation-regulated membrane localization of PiT2, ultimately reducing Pi transport (**B**); the p.S121C and p.S601W mutations in the PD domains impair the Pi-binding of PiT2, thereby contributing to PiT2 dysfunction (**C**). The curved thin black arrows indicate the transport of PiT2 to the cell membrane, the thin black arrows starting at AMPK or AKT indicate sites where they mediate PiT2 phosphorylation, and the red lines with bar ends indicate the inhibition of the mutation on the physiological process.

Correspondingly, patients with the p.S121C mutation showed very slight calcification and are all asymptomatic, patients with the p.S601W mutation exhibit more severe calcification and some are symptomatic, and affected individuals with compound heterozygous mutations show extremely extensive brain calcification and present with repetitive seizures and dysgnosia from infancy [7, 22]. Despite different pathogenesis, the p.T390A and p.S121C mutations had a similar effect on the Pi transport activity of PiT2 (Fig. 1). A patient with the homozygous p.T390A mutation had a relatively moderate phenotype compared with those carrying the compound heterozygous mutations (p.S121C and p.S601W), but she showed a relatively severe phenotype compared with her family members carrying the heterozygous p.T390A mutation [23]. The frameshift or nonsense mutations that could lead to the generation of truncated proteins or messenger RNA (mRNA) decay are usually more damaging to protein function than missense mutations [20, 45]. Patients with frameshift or nonsense mutations have been reported to present more severe brain calcification than those with missense mutations [46], which might result in an earlier onset and a higher proportion of clinical manifestations. Generally, the frameshift or nonsense mutations that are likely to cause the complete loss of the PiT2 function could be classified as the most severe type, and the associated patients might have the most severe phenotypes; the missense mutations that might result in either loss of function (such as p.S601W) or partially reduced transport function (such as p.S121C) could be classified as moderate or mild types, and the associated patients might have correspondingly moderate or mild phenotypes. Accordingly, the mutation severity might be positively correlated with the clinical phenotype to a certain degree.

Up to now, there has been no effective treatment for PFBC. Mutations in *SLC20A2* are a major cause of PFBC, accounting for as many as 61% of all cases with confirmed genetic forms [21]. Designing and screening for effective drugs targeting PiT2 will be of great importance for the treatment of PFBC. *SLC20A2* mutations have been linked to autosomal-dominant PFBC primarily caused by haploinsufficiency [7, 47]. Therefore, enhancing the function of WT PiT2 would likely be an effective therapy. There are two possible strategies: one is to increase the activity of

WT PiT2, and the other is to increase the membrane localization of PiT2. In this study, we found that PiT2 phosphorylation promotes its membrane localization, providing insights into the development of PFBC therapies.

In conclusion, we propose that missense mutations in PiT2-loop7 contribute to Pi dyshomeostasis through the phosphorylation-mediated regulation of cell surface expression. This study improves our understanding of PFBC pathogenesis and highlights the importance of loop7 in the function of PiT2.

Acknowledgments This study was mainly supported by the National Natural Science Foundation of China (31871262) and a Shanghai Municipal Science and Technology Major Project (2018SHZDZX05).

Conflict of Interest The authors claim that there are no conflicts of interest.

References

1. Collins JF, Bai L, Ghishan FK. The SLC20 family of proteins: Dual functions as sodium-phosphate cotransporters and viral receptors. Pflugers Arch 2004, 447: 647–652.
2. Murer H, Hernando N, Forster I, Biber J. Proximal tubular phosphate reabsorption: Molecular mechanisms. Physiol Rev 2000, 80: 1373–1409.
3. Miller DG, Edwards RH, Miller AD. Cloning of the cellular receptor for amphotropic murine retroviruses reveals homology to that for gibbon ape leukemia virus. Proc Natl Acad Sci U S A 1994, 91: 78–82.
4. Pedersen L, Johann SV, van Zeijl M, Pedersen FS, O'Hara B. Chimeras of receptors for gibbon ape leukemia virus/feline leukemia virus B and amphotropic murine leukemia virus reveal different modes of receptor recognition by retrovirus. J Virol 1995, 69: 2401–2405.
5. Kavanaugh MP, Miller DG, Zhang W, Law W, Kozak SL, Kabat D. Cell-surface receptors for gibbon ape leukemia virus and amphotropic murine retrovirus are inducible sodium-dependent phosphate symporters. Proc Natl Acad Sci U S A 1994, 91: 7071–7075.
6. Olah Z, Lehel C, Anderson WB, Eiden MV, Wilson CA. The cellular receptor for gibbon ape leukemia virus is a novel high affinity sodium-dependent phosphate transporter. J Biol Chem 1994, 269: 25426–25431.
7. Wang C, Li YL, Shi L, Ren J, Patti M, Wang T, *et al*. Mutations in SLC20A2 link familial idiopathic basal ganglia calcification with phosphate homeostasis. Nat Genet 2012, 44: 254–256.
8. Salaün C, Rodrigues P, Heard JM. Transmembrane topology of PiT-2, a phosphate transporter-retrovirus receptor. J Virol 2001, 75: 5584–5592.
9. Bøttger P, Pedersen L. Mapping of the minimal inorganic phosphate transporting unit of human PiT2 suggests a structure universal to PiT-related proteins from all kingdoms of life. BMC Biochem 2011, 12: 21.
10. Bøttger P, Pedersen L. The central half of Pit2 is not required for its function as a retroviral receptor. J Virol 2004, 78: 9564–9567.
11. Feldman SA, Farrell KB, Murthy RK, Russ JL, Eiden MV. Identification of an extracellular domain within the human PiT2 receptor that is required for amphotropic murine leukemia virus binding. J Virol 2004, 78: 595–602.
12. Bottger P, Pedersen L. Two highly conserved glutamate residues critical for type III sodium-dependent phosphate transport revealed by uncoupling transport function from retroviral receptor function. J Biol Chem 2002, 277: 42741–42747.
13. Tsai JY, Chu CH, Lin MG, Chou YH, Hong RY, Yen CY, *et al*. Structure of the sodium-dependent phosphate transporter reveals insights into human solute carrier SLC20. Sci Adv 2020, 6.
14. Ravera S, Virkki LV, Murer H, Forster IC. Deciphering PiT transport kinetics and substrate specificity using electrophysiology and flux measurements. Am J Physiol Cell Physiol 2007, 293: C606–C620.
15. Kavanaugh MP, Kabat D. Identification and characterization of a widely expressed phosphate transporter/retrovirus receptor family. Kidney Int 1996, 49: 959–963.
16. Pizzagalli MD, Bensimon A, Superti-Furga G. A guide to plasma membrane solute carrier proteins. FEBS J 2021, 288: 2784–2835.
17. Ma XX, Li X, Yi P, Wang C, Weng J, Zhang L, *et al*. PiT2 regulates neuronal outgrowth through interaction with microtubule-associated protein 1B. Sci Rep 2017, 7: 17850.
18. Hsu SC, Sears RL, Lemos RR, Quintáns B, Huang A, Spiteri E, *et al*. Mutations in SLC20A2 are a major cause of familial idiopathic basal ganglia calcification. Neurogenetics 2013, 14: 11–22.
19. Lemos RR, Ramos EM, Legati A, Nicolas G, Jenkinson EM, Livingston JH, *et al*. Update and mutational analysis of SLC20A2: A major cause of primary familial brain calcification. Hum Mutat 2015, 36: 489–495.
20. Shen Y, Shu S, Ren Y, Xia W, Chen J, Dong L, *et al*. Case report: Two novel frameshift mutations in SLC20A2 and one novel splice donor mutation in PDGFB associated with primary familial brain calcification. Front Genet 2021, 12: 643452.
21. Balck A, Schaake S, Kuhnke NS, Domingo A, Madoev H, Margolesky J, *et al*. Genotype-phenotype relations in primary familial brain calcification: Systematic MDSGene review. Mov Disord 2021, 36: 2468–2480.
22. Wang C, Xu X, Li LL, Wang T, Zhang M, Shen L, *et al*. Molecular mechanism of idiopathic basal ganglia calcification. Yi Chuan 2015, 37: 731–740.
23. Chen S, Cen Z, Fu F, Chen Y, Chen X, Yang D, *et al*. Underestimated disease prevalence and severe phenotypes in patients with biallelic variants: A cohort study of primary familial brain calcification from China. Parkinsonism Relat Disord 2019, 64: 211–219.
24. Rubino E, Giorgio E, Godani M, Grosso E, Zibetti M, Lopiano L, *et al*. Three novel missense mutations in SLC20A2 associated with idiopathic basal ganglia calcification. J Neurol Sci 2017, 377: 62–64.
25. Taglia I, Mignarri A, Olgiati S, Menci E, Petrocelli PL, Breedveld GJ, *et al*. Primary familial brain calcification: Genetic analysis and clinical spectrum. Mov Disord 2014, 29: 1691–1695.
26. Waterhouse A, Bertoni M, Bienert S, Studer G, Tauriello G, Gumienny R, *et al*. SWISS-MODEL: Homology modelling of protein structures and complexes. Nucleic Acids Res 2018, 46: W296–W303.
27. Wang DK, Liu Y, Myers EJ, Guo YM, Xie ZD, Jiang DZ, *et al*. Effects of Nt-truncation and coexpression of isolated Nt domains on the membrane trafficking of electroneutral Na^+/HCO_3^- cotransporters. Sci Rep 2015, 5: 12241.
28. Pan D, Barber MA, Hornigold K, Baker MJ, Toth JM, Oxley D, *et al*. Norbin stimulates the catalytic activity and plasma membrane localization of the guanine-nucleotide exchange factor P-Rex1. J Biol Chem 2016, 291: 6359–6375.
29. Cater RJ, Chua GL, Erramilli SK, Keener JE, Choy BC, Tokarz P, *et al*. Structural basis of *Omega*-3 fatty acid transport across the blood-brain barrier. Nature 2021, 595: 315–319.

30. Guemez-Gamboa A, Nguyen LN, Yang H, Zaki MS, Kara M, Ben-Omran T, *et al*. Inactivating mutations in MFSD2A, required for omega-3 fatty acid transport in brain, cause a lethal microcephaly syndrome. Nat Genet 2015, 47: 809–813.
31. Lee EE, Ma J, Sacharidou A, Mi W, Salato VK, Nguyen N, *et al*. A protein kinase C phosphorylation motif in GLUT1 affects glucose transport and is mutated in GLUT1 deficiency syndrome. Mol Cell 2015, 58: 845–853.
32. Ma T, Li L, Chen R, Yang L, Sun H, Du S, *et al*. Protein arginine methyltransferase 7 modulates neuronal excitability by interacting with NaV1.9. Pain 2022, 163: 753–764.
33. Chen Z, Lei C, Wang C, Li N, Srivastava M, Tang M, *et al*. Global phosphoproteomic analysis reveals ARMC10 as an AMPK substrate that regulates mitochondrial dynamics. Nat Commun 2019, 10: 104.
34. Xie F, Jin K, Shao L, Fan Y, Tu Y, Li Y, *et al*. FAF1 phosphorylation by AKT accumulates TGF-β type II receptor and drives breast cancer metastasis. Nat Commun 2017, 8: 15021.
35. Han F, Li CF, Cai Z, Zhang X, Jin G, Zhang WN, *et al*. The critical role of AMPK in driving Akt activation under stress, tumorigenesis and drug resistance. Nat Commun 2018, 9: 4728.
36. Walsh CT, Garneau-Tsodikova S, Gatto GJ Jr. Protein posttranslational modifications: The chemistry of proteome diversifications. Angewandte Chemie Int Ed 2005, 44: 7342–7372.
37. Xu D, You G. Loops and layers of post-translational modifications of drug transporters. Adv Drug Deliv Rev 2017, 116: 37–44.
38. Li Z, Dong W, Zhang X, Lu JM, Mei YN, Hu C. Protein kinase C controls the excitability of cortical pyramidal neurons by regulating Kv2.2 channel activity. Neurosci Bull 2022, 38: 135–148.
39. Xu Q, Cheng HW, He HQ, Liu ZR, He M, Yang HT, *et al*. Deglycosylation altered the gating properties of rNav1.3: Glycosylation/deglycosylation homeostasis probably complicates the functional regulation of voltage-gated sodium channel. Neurosci Bull 2008, 24: 283–287.
40. Guo XX, Su HZ, Zou XH, Lai LL, Lu YQ, Wang C, *et al*. Identification of SLC20A2 deletions in patients with primary familial brain calcification. Clin Genet 2019, 96: 53–60.
41. Deng D, Xu C, Sun P, Wu J, Yan C, Hu M, *et al*. Crystal structure of the human glucose transporter GLUT1. Nature 2014, 510: 121–125.
42. Bai G, Zhang M. Mesophasic assembly of inhibitory postsynaptic density. Neurosci Bull 2021, 37: 141–143.
43. Salaün C, Maréchal V, Heard JM. Transport-deficient Pit2 phosphate transporters still modify cell surface oligomers structure in response to inorganic phosphate. J Mol Biol 2004, 340: 39–47.
44. Bøttger P, Pedersen L. Evolutionary and experimental analyses of inorganic phosphate transporter PiT family reveals two related signature sequences harboring highly conserved aspartic acids critical for sodium-dependent phosphate transport function of human PiT2. FEBS J 2005, 272: 3060–3074.
45. Supek F, Lehner B, Lindeboom RGH. To NMD or not to NMD: Nonsense-mediated mRNA decay in cancer and other genetic diseases. Trends Genet 2021, 37: 657–668.
46. Guo XX, Zou XH, Wang C, Yao XP, Su HZ, Lai LL, *et al*. Spectrum of SLC20A2, PDGFRB, PDGFB, and XPR1 mutations in a large cohort of patients with primary familial brain calcification. Hum Mutat 2019, 40: 392–403.
47. Cassinari K, Rovelet-Lecrux A, Tury S, Quenez O, Richard AC, Charbonnier C, *et al*. Haploinsufficiency of the primary familial brain calcification gene *SLC20A2* mediated by disruption of a regulatory element. Mov Disord 2020, 35: 1336–1345.